Elastic converted-wave path migration for subsalt imaging

Ru-Shan Wu, Rui Yan, Xiao-Bi Xie, Modeling and Imaging Laboratory, Earth and Planetary Sciences/IGPP, University of California, Santa Cruz, David Walraven, Anadarko Petroleum Corp.*

Summary

Using a simple salt layer elastic model with both flat and steep faults at the subsalt area, we demonstrated the concepts and method of selected C-path (converted-wave path) imaging to improve the subsalt illumination and reduce migration artifacts. First we investigate the survey efficiency of different C-paths through energy budget evaluation for different incident and scattering paths. Then we test the image quality for different migration C-paths. By using C-paths with at least one S-segment inside the salt body, the blind area of pure P-wave imaging for steep subsalt faults having dip larger than the critical angle (37^0) was eliminated. Using different C-path combinations can also substantially reduce the elastic migration artifacts caused by path-mismatches between the data and migration. Further study for eliminating the conversion mismatch artifacts is needed.

Introduction

The large velocity contrast across the sedimentary/salt interfaces, which are often irregular in shape, is a major obstacle that prevents seismic waves from penetrating the salt body, resulting in poor subsalt images. Especially for the steep faults beneath salt body, the deadly critical/post-critical reflections of P-waves may put these reflectors totally in the blind zone of P-wave survey. It is known that the converted-wave can penetrate the salt body and reach the blind zone of P-wave survey (Purnell, 1992; Li et al., 1998; Jones and Gaiser, 1999). Previous attempt of using converted-wave path (C-path) imaging to improve the P-wave illumination adopted scalar wave propagators for both P- and S-waves and demonstrated the idea using a post-stack migration of the 2D SEG/EAGE salt model (Wu et al., 2001). Although the steep subsalt reflectors, missing in the conventional P-wave imaging, appeared in the C-path image, however, strong artifacts in the image may be caused by the use of scalar propagator along the C-paths. Also the use of scalar wave propagator for elastic wave extrapolation is dynamically incorrect. In this study we expand the previous study and address two issues in pre-stack migration using converted-wave paths. First we investigate the survey efficiency of different C-paths through energy budget evaluation for different incident and scattering paths; second, we demonstrate the concept and method of prestack C-path imaging by using a simple salt-layer model. As an elastic wave propagator, we developed a hybrid one-way propagator using a combination of R/T (reflection-transmission) method and an elastic Born modeling operator.

ENERGY PARTITION OF DIFFERENT C-PATHS FOR SUBSALT SURVEY

In this study, we are mainly concerned with subsalt imaging in the poorly illuminated region of conventional imaging methods. Especially we are targeted at steep subsalt reflectors which are totally invisible by the conventional P-P imaging. These reflectors have only weak elastic parameter contrasts from the surrounding media. Let us first look at the energy partition between P and S scattering (reflection) as a function of incident angles (Figure 1). We know that for these steep faults, the recorded P-to-S reflections from targets are mainly from near-normal, incident waves due to the acquisition aperture limitation. For these near-normal events, their reflection angles (the angle between the incident direction and the reflector normal) are very small. Under this circumstance, the P-S conversion coefficient is much weaker than that of P-P reflection (Figure 1). Hanssen and Li (2000) has noticed the weakness of the C-wave events and pointed out the difficulty in utilizing theses events for sub-basalt converted-wave imaging. This conclusion is for the conventional CCP (common-conversion-point) migration. However, as pointed out by Wu et al. (2001), the strong P-P reflection at small angles can penetrate the salt body along some converted-wave path (C-path) and reach the geophones on the surface. This can be seen clearly from C-path transmission presented in Figures 2, 4 and 5.

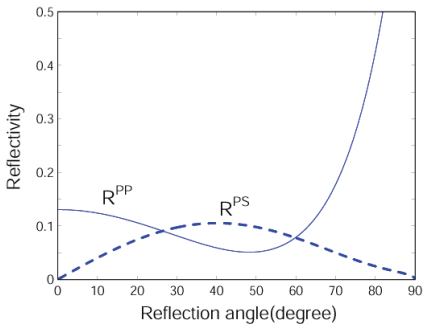

Figure 1. P-P (solid line) and P-S (dashed line) reflectivity on a reflector (fault). Note that at small reflection angles (the angle between the incident direction and the reflector normal), e.g., near normal incidence, the P-to-S reflectivity (conversion coefficient) is very weak in comparison with P-P reflectivity.

Figure 2a and 2b show different paths of converted waves in penetrating a salt layer and their energy transmission coefficients, respectively. The medium parameters of the

salt layer are $V_P = 4.48km/s$, $V_S = 2.6km/s$, $\rho = 2.1g/cm^3$ and the sediments are $V_P = 2.59km/s$, $V_S = 1.5km/s$, $\rho = 2.2g/cm^3$. Due to the huge velocity contrast between the sediments and salt bodies, the P-wave path can only pass through the salt bodies within the range of critical incidence, and the waves beyond the critical angle are completely blocked, resulting in various shadow zones (or blind areas) for subsalt imaging. We see that for small angles, the paths PPP and PPS carry most of the energy; however, beyond the critical angle, only the paths with an S-segment inside the salt body (paths PSP and PSS) can carry the energy through salt. This Figure gives us the basic idea of subsalt illumination with different C-paths.

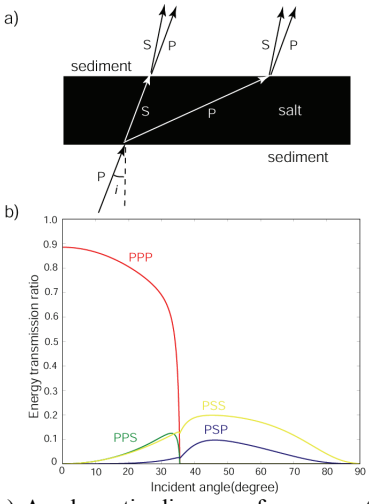

Figure 2. a) A schematic diagram of one-way transmitted wave paths penetrating through a salt layer. b) Energy transmission coefficients for different wave paths.

Now we discuss the path efficiency for subsalt imaging when steep reflectors are targeted. Figure 3 plots a schematic diagram of converted wave paths that provide illumination to a 45°-dip subsalt fault. Figure 4 and 5 present the path efficiency for subsalt imaging of this target. The calculation can be easily done by integrating the information in Figure 1 and 2. The paths are labeled with two legs such as PPP-PSP. The left leg (PPP) is the source side path and the right leg (PSP) is the receiver side leg. The efficiency is expressed in term of energy ratio between the received and the radiated energy fluxes on the surface. The total energy loss includes the path transmission loss and the reflection ratio (reflection coefficient). Figure 4 shows the efficiency as a function of incident angle at the surface. We see that the energy of PPP-PSP(or S) is limited to small incident angles and peaked just before the critical angle, in this case is around 30^0; the energy of PSP-PSP(or S) is distributed at medium incident angle (40^0-50^0); the energy of PSS-PSP(or S) spreads at large incident angles with small magnitude because of the low S-P conversion ratio at the fault. Figure 5 shows the efficiency as a function of offset normalized by the depth, which is proportional to the open angle. We see that the paths with only one S-segment in the salt have greater efficiency and broader spread over open angles; the paths with two S-segments in the salt have smaller efficiency and offset spread, but they still carry enough energy to be useful.

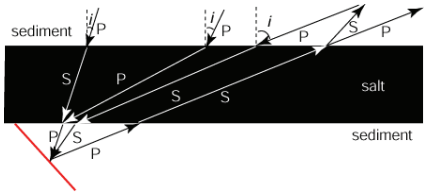

Figure 3. A schematic diagram of converted wave paths that provide illumination to a 45°-dip subsalt fault.

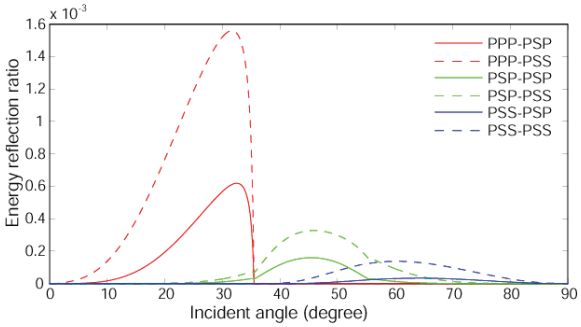

Figure 4. Path efficiency as a function of incident angle for steep fault illumination as shown in Figure 3.

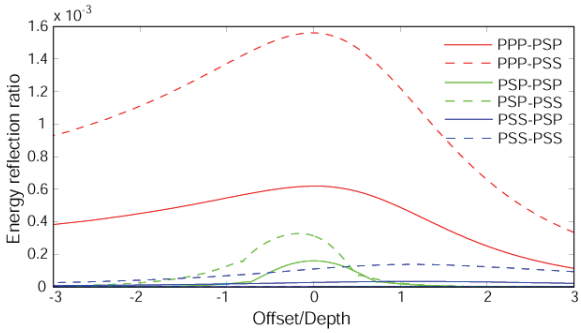

Figure 5. Path efficiency as a function of offset (normalized by reflector depth) for steep fault illumination as shown in Figure 3.

NUMERICAL TESTS ON C- PATH MIGRATION FOR STEEP SUBSALT FAULTS

Elastic model and synthetic data: In order to demonstrate the idea and feasibility of converted-wave path (C-path)

imaging, we generate a synthetic data set and perform the C-path migration for a simple model. The model is composed of both steep subsalt reflector and a flat subsalt baseline beneath a salt layer (Figure 6). Even though the salt layer is not representative of the real salt structure and much simplified the wave scattering when penetrating the salt body, the fundamental nature of critical reflection and P-wave shadowing is kept. So the characteristics of C-path imaging can be easily seen and understood from this example.

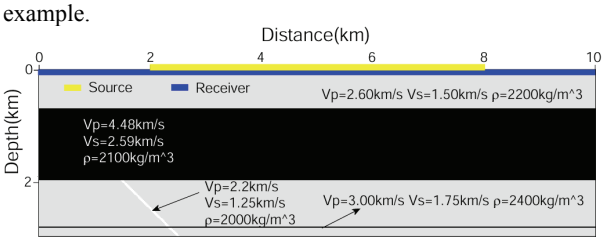

Figure 6. A simple salt layer model with two subsalt reflectors: A steep (45^0 fault) and a flat baseline reflector. The source and receiver distributions on the surface are also sketched.

We developed a hybrid reflection/transmission (R/T) – Born method for both the modeling and migration. At the salt boundaries, both top and bottom, we calculate the elastic transmission and reflection coefficients by Zoeppritz equation, which can be considered as exact one-way elastic propagator for the salt layer. For the subsalt faults, which has weak perturbations in parameters (shown in Figure 6), we use the local Born approximation, which includes incident field updating by forward scattering (see Wu et al, 2007). This hybrid method is considered as an accurate elastic one-way propagator for this model. We compared the synthetic seismograms by our hybrid method to those generated by an elastic finite difference algorithm. They have excellent agreement. Therefore we have the confidence on the test results using this propagator.

Elastic migration with selected C-paths: We carry out a seismic experiment with 41 shots spaced 0.15km starting at 2km. There are 500 receivers for each shot in a fixed-spread configuration. The interval between receivers is 0.02km. For the migration, we use the R/T propagator as the one-way elastic migration operator. For one-way elastic propagator in general, it has the flexibility of switching on/off different elastic scattering modes among P-P, P-S, S-P and S-S at each sediment-salt interface. In this way, we can control the C-path in the migration operator, and have the capability of matching the signal of different C-paths in the data. We apply the elastic vector imaging condition to stack the backpropagated wavefield at $t_s = t_g$. Figure 7 shows the comparison of conventional elastic migration (RTM) (top panel), P-P migration (mid panel), and the C-path migration using PSP-PPP and PPP-PSP paths (bottom panel). To see the details of subsalt images, only the subsalt part of the image is shown in the figures. We see that P-wave only migration has a blind zone for steep subsalt imaging (in this case is about dip > 37^0) (Figure 7b). While the conventional elastic migration can image the steep fault, however, the artifacts alongside the true faults are hard to recognize and remove (Figure 7a). In comparison, the C-path image using selected C-paths (PSP-PPP and PPP-PSP) can separate the true image from the artifacts (Figure 7c).

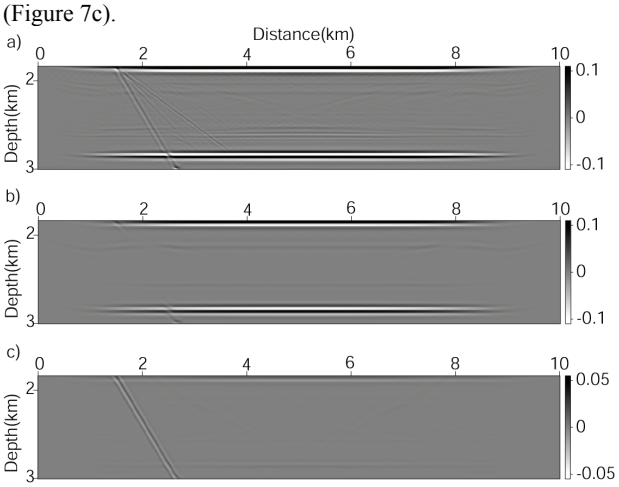

Figure 7. Comparison of a) conventional elastic migration (RTM) (top panel), b) P-P migration (mid panel), and c) the C-path migration using PSP-PPP and PPP-PSP paths (bottom panel). On the panels only the subsalt part of image is shown.

To understand the artifacts generated by conventional elastic migration (e.g. RTM), we show several examples of path mismatch (Figure 8). In Figure 8a, we generate the synthetic seismograms using our hybrid method, but with only the PSP-PSP path switched on. If the migration operator contains a different path, such as PSS-PSP, then the travel time of the backpropagation from the left-leg (PSS) will mismatch the left-leg of the data (PSP), resulting in a false image with wrong location and wrong dip. The second example (Figure 8b) shows the mismatch between PSS-PSP (signal) and PSP-PSP (migration). In the third example (Figure 8c), the path in the data is PPP-PSP, but the migration path is PSP-PSP. All the mismatches between the data-path and migration-path produce false images as artifacts. Since the RTM operator contains all the possible paths, the artifacts generated are difficult to recognize and separate. In an ideal acquisition of 360^0 coverage, these artifacts of mismatch will be cancelled by interference. In the case of limited surface acquisition, these artifacts are inevitable. In comparison, the selected C-path migration

provides the flexibility for migration path selection, and therefore can reduce the artifacts substantially. Of course, the C-path migration cannot eliminate all the mismatches, therefore cannot remove all the artifacts for complex models. Figure 9 shows the test with a three subsalt faults of different dips: 45^0, 30^0 and 15^0 (Figure 9a). Figure 9b gives the pure P-path migration. As expected, the steep fault of 45^0 is missing. Figure 9c gives the image using all the paths and regular imaging condition; Image in Figure 9d uses all the paths but applies only the P-P imaging condition in the subsalt area. Figure 9e is from the path combination of PPP-PSP and PSP-PPP. Figure 9d and 9e present the best images using different path combinations for this particular example. We see images of all the faults. However, there exist still artifacts which cannot be removed by simple path selection. For more complicated cases, the artifacts may behave differently. Nevertheless, the C-path imaging can substantially reduce the artifacts and provides the image attributes for further separating artifacts from true reflections and for other applications.

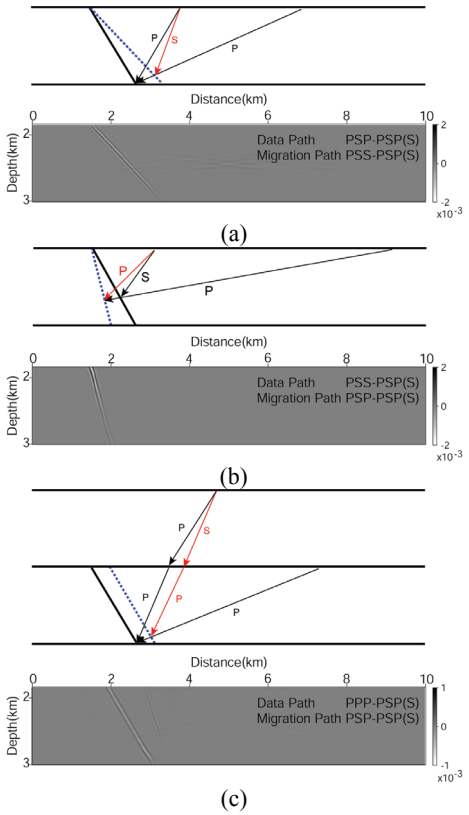

Figure 8. Examples of path mismatch between the data and the migration operator.

Conclusions

Using a simple salt layer elastic model with both flat and steep faults at the subsalt area, we demonstrated the concepts and method of selected C-path (converted-wave path) imaging to improve the subsalt illumination and reduce migration artifacts. By using C-paths with at least one S-segment inside the salt body, the blind area for steep subsalt faults having dip larger than the critical angle (37^0) was eliminated. Using different C-path combinations can also substantially reduce the migration artifacts caused by mismatch between the data and migration. However, there are still exist artifacts which cannot be removed by simple path selection. Nevertheless, the C-path imaging provides the image attributes for further separating artifacts from true reflections and for other applications. For future study we will develop and improve one-way elastic propagators for C-path imaging applying to highly irregular salt bodies.

Acknowledgements

We thank the support of DEEPSTAR for this research project. Help and contribution from Yingcai Zheng is appreciated.

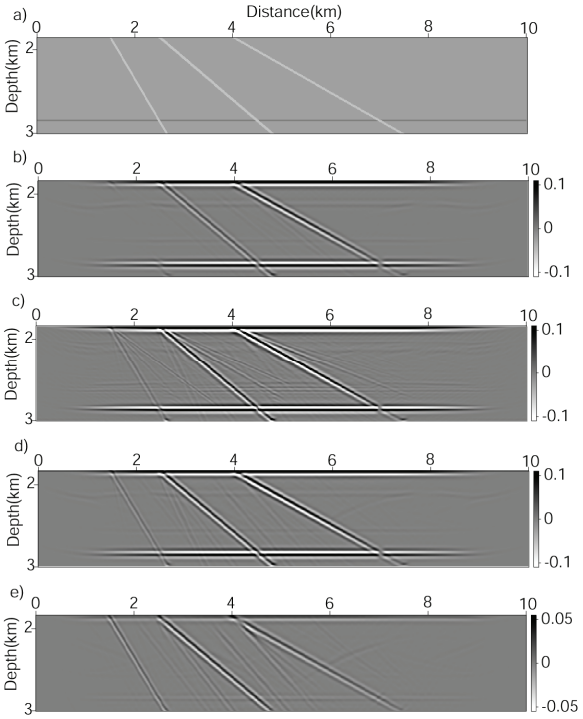

Figure 9 a) The velocity model**;** ; b) Migrated image with only pure P-path for the whole model; c) Switching on all the wave paths during migration but apply only the P-P imaging condition at the subsalt region; d) Migrated image with PPP-PSP and PSP-PPP path combination.

EDITED REFERENCES

Note: This reference list is a copy-edited version of the reference list submitted by the author. Reference lists for the 2010 SEG Technical Program Expanded Abstracts have been copy edited so that references provided with the online metadata for each paper will achieve a high degree of linking to cited sources that appear on the Web.

REFERENCES

Hanssen, P., X. Y. Li, and A. Ziolkowski, 2000, Converted waves for sub-basalt imaging?: 70th Annual International Meeting, SEG, Expanded Abstracts, MC 2.3.

Jones, N., and J. Gaiser, 1999, Imaging beneath high-velocity layers, Expanded Abstracts of the Technical Program: 69th Annual meeting, SEG, 713-716.

Li, X. Y., C. MacBeth, K. Hitchen, and P. Hanssen, 1998, Using converted shear waves for imaging beneath basalt in deep water plays: 68th Annual meeting, SEG, Expanded Abstract of the Technical Program, 1396-1372.

Purnell, G. W., 1992, Imaging beneath a high-velocity layer using converted wave: Geophysics, **57**, 1444–1452, doi:10.1190/1.1443212.

Wu, R. S., H. Guan, and X. Y. Wu, 2001, Imaging steep sub-salt structure using converted wave paths, Expanded Abstract of the Technical Program: 71st Annual meeting, SEG.

Wu, R. S., X. B. Xie, and X. Y. Wu, 2007, One-way and one-return approximations for fast elastic wave modeling in complex media, *in* R.S. Wu and V. Maupin, Advances in Wave Propagation in Heterogeneous Earth: Elsevier, 266-323.